sustainability

MDPI

Article

Effects of Tb-Doped $BiVO_4$ on Degradation of Methylene Blue

Wei-Sheng Chen [1], Ming-Hong Wu [1,*] and Jun-Yi Wu [2,*]

[1] Department of Resources Engineering, National Cheng Kung University, No. 1, University Rd., East District, Tainan 70101, Taiwan; kenchen@mail.ncku.edu.tw
[2] Department of Intelligent Automation Engineering, National Chin-Yi University of Technology, No. 57, Sec. 2, Zhongshan Rd., Taiping District, Taichung 411030, Taiwan
* Correspondence: n46101244@gs.ncku.edu.tw (M.-H.W.); wu8053@ncut.edu.tw (J.-Y.W.); Tel.: +886-62-757575 (ext. 62828) (M.-H.W.)

Abstract: Bismuth vanadate ($BiVO_4$) is a narrow-bandgap semiconductor (~2.41 Ev) that responds to visible light. The efficiency of degradation of organic dyes is indexed by methylene blue (MB). After 150 min, the efficiency of MB degradation by pure $BiVO_4$ was about 20%. Its adsorption performance and electron–hole pair migration ability are weak, and the photocatalytic activity of pure $BiVO_4$ needs to be improved. $BiVO_4$ doped with rare earth ions can facilitate the separation of photogenerated electron–hole pairs, thereby enhancing photocatalytic activity in the visible light range. This study investigates changes in the structure and morphology of $BiVO_4$ doped with different atomic percentages of terbium (Tb). $BiVO_4$ powders were prepared by the hydrothermal method with different atomic percentages of Tb (at% = 0, 1, 3, and 5). Doping Tb benefits the coexistence of monoclinic/tetragonal heterostructures, which changes the band gap and improves degradation efficiency. After 150 min of visible light irradiation, the photocatalyst doped with 3 atomic percent of Tb exhibited 98.2% degradation of methylene blue. The degradation percentage of MB remained stable in the presence of 3at%Tb-doped $BiVO_4$ composite. The optimal parameters for the amount of photocatalyst added were studied. Real-field simulations of metal ions and inorganic salts both retain high levels of degradation efficiency.

Keywords: $BiVO_4$; photocatalysts; degradation; organic dyes

Citation: Chen, W.-S.; Wu, M.-H.; Wu, J.-Y. Effects of Tb-Doped $BiVO_4$ on Degradation of Methylene Blue. *Sustainability* **2023**, *15*, 6994. https://doi.org/10.3390/su15086994

Academic Editor: Agostina Chiavola

Received: 9 March 2023
Revised: 15 April 2023
Accepted: 18 April 2023
Published: 21 April 2023

1. Introduction

The development of global industrialization has brought people a more prosperous and convenient life, but it is accompanied by the gradual depletion of energy and the problems of environmental pollution [1,2]. The need for diversification and sustainability of energy use and the development of clean and sustainable energy has become a consensus of the modern world.

Solar energy is clean, pollution-free green energy. Many studies have been devoted to how to effectively utilize solar energy in the fields of energy and industrial applications [3,4]. Among them, the photocatalytic effect in semiconductors using solar energy as an energy source has been widely valued and deeply researched and explored since the publication of the Honda Fuji effect in 1972 [5]. The applications of the photocatalytic reaction include scraping treatment of dyes, pesticides, microbial germs, and so on to achieve water disinfection and purification. Emission reduction treatments of toxic and greenhouse gases, such as reducing acid rain by oxidizing nitrogen oxides NO_X, reducing CO_2 to hydrocarbons to perform chemical carbon sequestration, and producing clean energy hydrogen through photohydrolysis, are all photocatalytic environmental purifications and have potential for development in energy production [6,7]. Titanium dioxide is also widely known among photocatalysts due to its photocatalytic activity, non-toxicity, high photostability, and long-term development [8–11]. However, due to the disadvantage of its wide bandgap (3.2 eV for anatase), TiO_2 cannot utilize the wavelengths of visible light,

while ultraviolet radiation accounts for only about 4% of sunlight [12–14]. Compared to TiO_2, which can only be excited by ultraviolet radiation, $BiVO_4$ has an obvious visible light response; this is a narrow bandgap semiconductor (~2.41 eV) and has advantages, but $BiVO_4$ has the disadvantages of poor adsorption performance and photocatalytic activity with fast photogenerated electron–hole recombination [15–17]. Solutions include metal doping, non-metal doping, rare earth doping, semiconductor coupling, etc. [15,18–20]. Among them, it is an excellent strategy to dope the Bi site of $BiVO_4$ with rare earth ions [21]. Because of its unique electronic transition characteristics and abundant energy levels, it suppresses the carrier recombination rate [22–24].

From the research of other scholars, it can be found that rare earth ion doping of $BiVO_4$ can produce superior visible light activity [25–27]. For instance, the ability of terbium ions to trap photoexcited electrons in the conduction band to reduce the electron–hole recombination rate is valued. Therefore, Tb-doped $BiVO_4$ was chosen to increase its photocatalytic activity to degrade organic pollutants [26–28]. In this study, a Tb-doped $BiVO_4$ photocatalyst was prepared by the hydrothermal method. This study is the first to introduce terbium doping into bismuth vanadate under acidic conditions and investigates its degradation using various concentrations of methylene blue in different environments. Sample analysis determines its crystal structure, valence state, specific surface area, and appearance with different atomic percentages of Tb doping. Its photocatalytic performance can be evaluated by degrading MB with the Tb-doped $BiVO_4$ photocatalyst under visible light irradiation. A further step changes the degradation efficiency of the methylene blue solution of the photocatalyst in different environments and confirms whether it still maintains good degradation efficiency [29]. The purpose is to make it conform to the application requirements of field dyes and contribute to the development of green energy materials.

2. Materials and Methods

2.1. Reagents and Materials

Bismuth (iii) nitrate pentahydrate ($Bi(NO_3)_3{\cdot}5H_2O$) (99%), ammonium vanadium oxide (NH_4VO_3) (99%), terbium (iii) nitrate hydrate (Tb $(NO_3)_3{\cdot}6H_2O$) (99.99%), and methylene blue (MB). All precursor materials were purchased from Sigma-Aldrich. Ethanol and deionized water were applied in all processes.

2.2. Characterization Methods

X-ray diffractometer (XRD) analysis was performed on an X-ray diffractometer (X-ray Diffraction Meter, Dandong, China, DX-2700) with Cu Kα radiation (λ = 0.15418 nm). Brunauer–Emmett–Teller (BET) surface area and pore structure were analyzed by adsorption and desorption with nitrogen at 77 K (Micromeritics ASAP 2020 specific surface analyzer). To demonstrate the presence of chemical bonds on the surface and accurate atomic % on the surface, the end products were analyzed by X-ray photoelectron spectroscopy (XPS) applied with a PHI 5000 VersaProbe (A & B ANALYTICAL & BIO SCIENCE INSTRUMENTS Co., Ltd., Taipei, Taiwan). To confirm the overall morphology and uniformity of the particles, products were inspected by a multi-function environmental field emission scanning electron microscope (FE-SEM) (Carl Zeiss AG, Jena, Germany) operating at 10 kV. UV−visible absorption spectra were taken using a HITACHI U4100 (E HONG INSTRUMENTS Co., Ltd., Taipei, Taiwan) at room temperature.

2.3. Preparation of Photocatalysts

Pure $BiVO_4$ and Tb-doped $BiVO_4$ samples with different atomic percentages were prepared by a simple hydrothermal method with the same temperature and duration. $Bi(NO_3)_3{\cdot}5H_2O$(0.02 mol) was dissolved into 3.0 mol/L HNO_3 solution (50 mL) and vigorously stirred at room temperature for 30 min to form transparent solution A. Next, NH_4VO_3(0.02 mol) was dissolved into 3.0 mol/L NaOH solution (50 mL) and stirred for 30 min at room temperature to prepare transparent solution B with vigorous stirring at

room temperature. Solution B was slowly added to solution A to form a solution with a yellow precipitate, which was put into an ultrasonic shaker for ten minutes to mix evenly. Afterwards, the pH value of the mixed solution was adjusted to 4 using low concentrations of NaOH and HNO_3. The mixed solution was poured into an autoclave, and the reaction temperature and time were 180 °C and 6 h. The resulting precipitate was washed several times with distilled water and ethanol to remove organic impurities, and the samples were dried in an oven at 80 °C for 24 h [30]. Undoped $BiVO_4$ can then be obtained. To prepare different atomic percentages of Tb-doped $BiVO_4$ in this study, when preparing solution B, different contents of $Tb(NO_3)_3{\cdot}6H_2O$ were added into the solution. The molar ratios of Tb and Bi are 1, 3, and 5 at%. Tb-$BiVO_4$ doped with different atomic percentages can be obtained. Figure 1. Experimental Procedure Diagram.

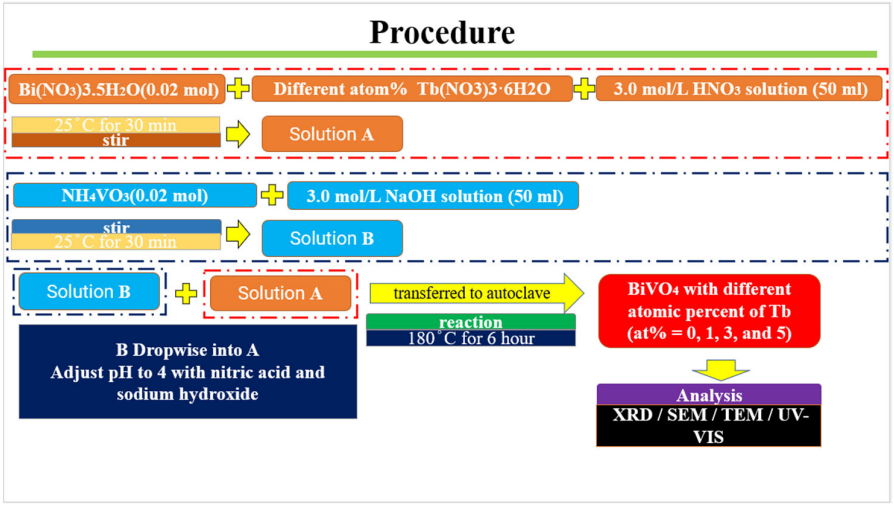

Figure 1. The experiment process.

2.4. Photocatalysis Analysis

The photocatalytic performance of $BiVO_4$ samples doped at different atomic percentages was evaluated using the degradation rate of the organic dye MB under visible light (400 W xenon lamp, light intensity 150 mW/cm^2). The initial concentration of MB solution was 10 ppm, and the pH was 7. A total of 15 mg of photocatalyst was added to 10 mL MB solution. Before illumination, the solution was magnetically stirred for 30 min in the dark to ensure the adsorption–desorption equilibrium. The suspension was then exposed to visible light irradiation (400 W Xenon lamp) under magnetic stirring. Subsequently, we extracted 1 mL of the reaction solution to separate out the photocatalyst using a centrifuge. The UV-Vis absorption spectrum of 1 mL of the reaction solution was detected at 30, 60, 90, 120, and 150 min, including the corresponding absorbance concentration changes at the characteristic peak (665 nm) of MB [31]. The amount of photocatalyst added (5, 10, 15, 20, and 25 mg), the initial concentration of organic dyes (5, 10, 15, 20, and 25 ppm), the addition of metal ions and inorganic salts (1.5, 3, and 4.5 g/L), and MB initial pH (5, 6, 7, 8, 9, and 10) were varied for analysis. To further explore the photocatalytic activity, the normalized rate constant (k_n) was obtained from the apparent rate constant. The apparent rate constant (k_a) of the degradation reaction was followed by a pseudo first-order equation and calculated using Equation (1) [31]:

$$\ln\left(\frac{C_0}{C_t}\right) = k_a t \quad (1)$$

In this equation, C_0 is the initial concentration of the organic dye, C_t is the concentration of the organic dye at a certain time, and t is time (min). The organic dyes here all use MB.

The specific surface areas of the composite materials are not the same. Samples with larger specific surface areas are more efficient at absorbing surrounding molecules per unit of time. This increases their photocatalytic efficiency. In order to further normalize

the corresponding specific surface area, the apparent rate constants (k_a) of the composites are divided by their specific surface areas. The normalized rate constant (k_n) is given by Equation (2) [31]:

$$k_n = \frac{k_a}{S_{BET}} \quad (2)$$

The specific surface area of each composite is expressed as S_{BET} (BET surface area). The percent degradation uses Equation (3) [31]:

$$\% \text{ degradation} = \frac{c_0 - c_t}{C} \times 100\% \quad (3)$$

3. Results and Discussions

3.1. Structural Characterization

Tb-doped $BiVO_4$ samples with different atomic percentages were obtained by hydrothermal synthesis for all the following analyses and discussions. In previous studies, Yaohong Zhang et al. demonstrated that, when rare earth ions are Y-doped into $BiVO_4$, the crystal system changes [23]. The XRD patterns of four doped samples with different atomic percentages in this study are shown in Figure 2. It is easy to see that the standard card [ICSD card number 100603] of single-crystal $BiVO_4$ is the same as the main diffraction peak of undoped $BiVO_4$ [32]. At this time, the lattice of space group I2/b of monoclinic $BiVO_4$ has constants a = 5.215 Å, b = 5.084 Å, and c = 11.706 Å. When the amount of rare earth ion Tb^{3+} increases to 1 atomic percent, the characteristic peak of tetragonal $BiVO_4$ will be observed at 24.54° [ICSD Card No. 100733]. When the atomic percentage increases to 3, there are more obvious characteristic peaks. Thus, there is a mixed phase of monoclinic and tetragonal $BiVO_4$ [32]. When the content of rare earth ion Tb^{3+} increases to 5 atomic percent, it can be seen from the XRD spectrum that the system monoclinic disappears. The characteristic peaks show that it has become the tetragonal crystal system of $BiVO_4$. It is known that doping Tb will stabilize $BiVO_4$ towards the tetragonal crystal system.

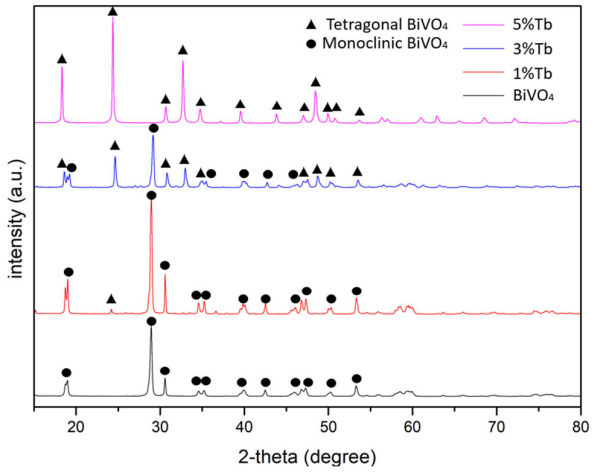

Figure 2. The XRD patterns of all samples.

The surface areas of the prepared samples were tested using N2 physisorption/desorption, and the results are presented in Table 1. It can be seen from the BET results that the surface area of the monoclinic sample is lower compared to that of the tetragonal system. The crystal phase transition occurs when Tb^{3+} is doped, and the surface area increases with increasing atomic percentage [33].

Table 1. Specific surface areas of the fabricated samples.

BET	$BiVO_4$	1%Tb	3%Tb	5%Tb
Surface Area	4.41	5.34	5.63	5.72

Figure 3a shows the full XPS spectra of pure $BiVO_4$ and 3at%Tb-$BiVO_4$ as representative of doped samples. In Figure 3b, it can be seen that the binding energies of the pristine $BiVO_4$ samples at the Bi($4f^{5/2}$) and Bi($4f^{7/2}$) core levels exist at 164.43 and 159.0 eV [34]. In the XPS spectrum of Figure 3c, the deconvoluted peak at 156.39 eV for the 3at%Tb-$BiVO_4$ sample can be judged to be in the Tb 4d orbital, indicating that terbium exists in the Tb^{3+} state [35]. In addition, the binding energy of V 2p showed almost no difference between $BiVO_4$ and 3at%Tb-$BiVO_4$ (Figure 3d,e). The two peaks at 529.5 and 531.3 eV are due to the relationships between lattice oxygen (O1s) $BiVO_4$ crystals and –OH groups formed on the surfaces of the two samples, respectively (Figure 3f,g) [30]. Since no impurity phase containing Tb^{3+} ions was found in XRD, XPS research shows that Tb^{3+} can exist in Bi^{3+} sites. Table 2 shows the XPS fitting parameters of $BiVO_4$ and 3%Tb.

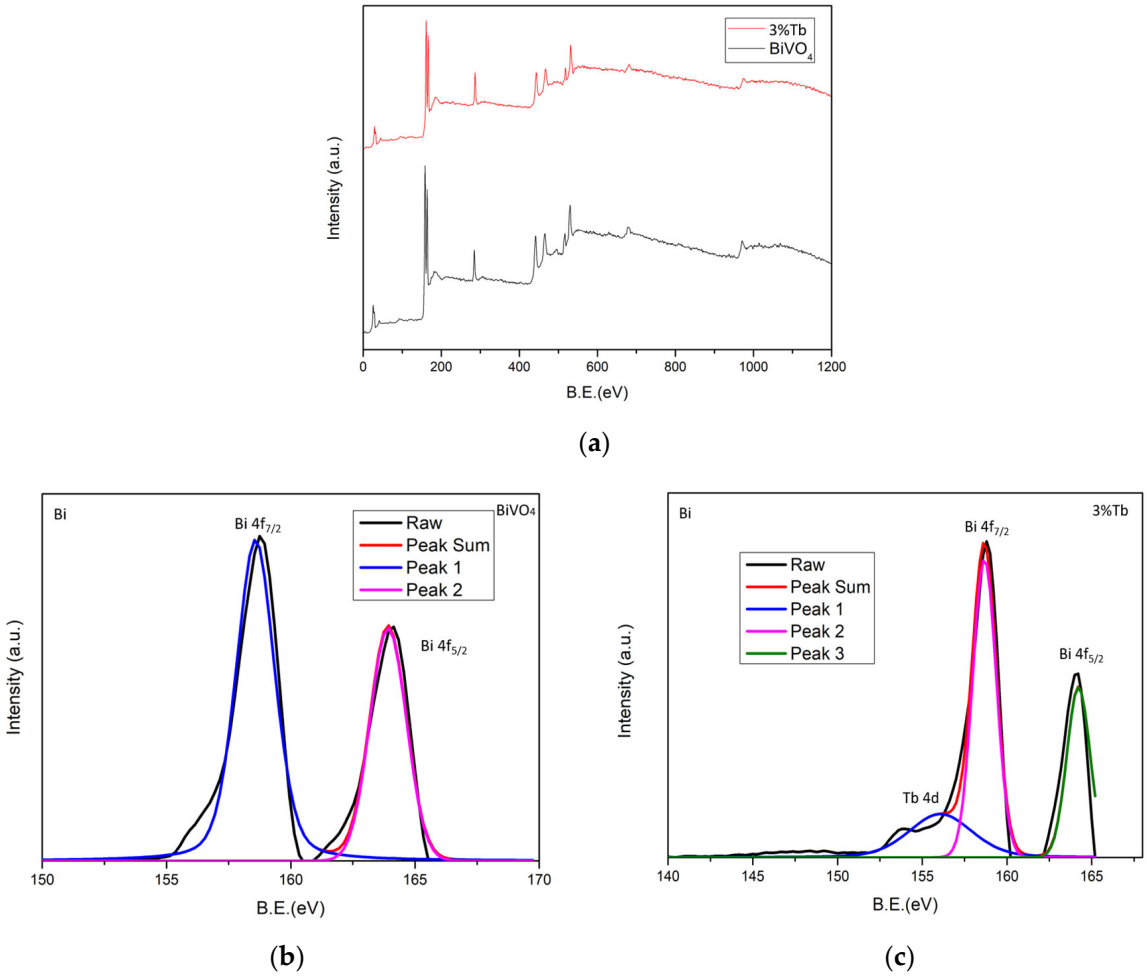

Figure 3. *Cont.*

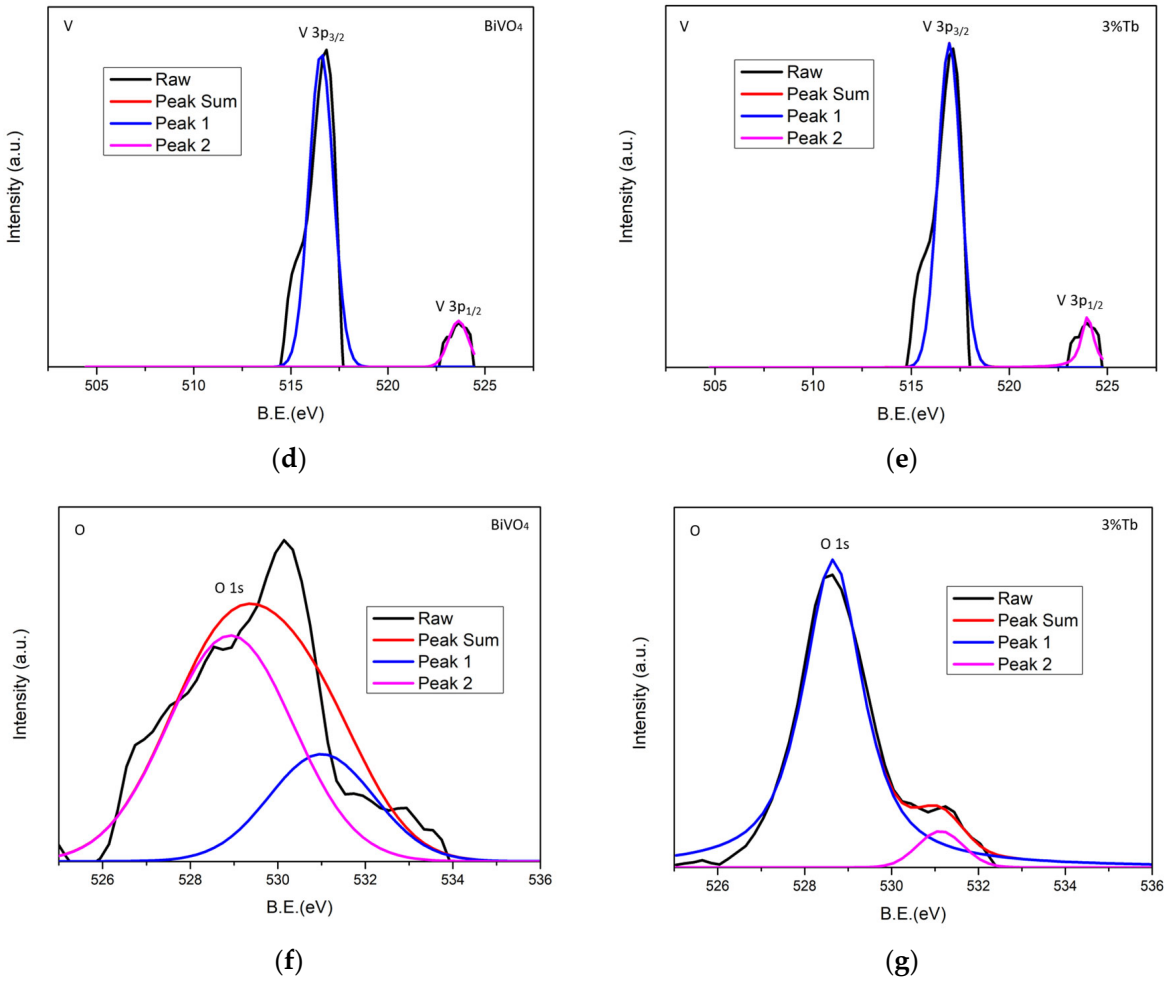

Figure 3. X-ray photoelectron spectroscopy (XPS): XPS full spectra of (**a**) $BiVO_4$ and 3%Tb-$BiVO_4$; (**b**) $BiVO_4$ Bi4f; (**c**) 3%Tb-$BiVO_4$ Bi4f; (**d**) $BiVO_4$ V3p; (**e**) 3%Tb-$BiVO_4$ V3p; (**f**) $BiVO_4$ O1s; and (**g**) 3%Tb-$BiVO_4$ O1s.

Table 2. XPS fitting parameters of $BiVO_4$ and 3%Tb.

Sample	Bi Peak ($4f_{7/2}$, $4f_{5/2}$)	Tb Peak (4d)	V Peak ($3p_{3/2}$, $3p_{1/2}$)	O Peak (1s)
$BiVO_4$	164.43, 159.0	none	517, 523	529.5, 531.3
3%Tb	158.78, 164.08	156.39	516.75, 524.16	529.42, 530.51

3.2. Surface Morphology

All fabricated sample morphologies were determined by SEM analysis. Described by Malathi et al., the shapes of $BiVO_4$ prepared by different processes are also different [36]. This includes the use of hydrothermal synthesis of additive-free $BiVO_4$ (140 °C/6 h, 100 °C/20 h, 100 °C/12 h, 180 °C/10 h, 170 °C/4 h, and 180 °C/24 h). The shapes they presented were octahedra, needles, dendrites, hollow spheres, spheres, and olive-like hierarchical shapes. The hydrothermal synthesis of additive-free pure $BiVO_4$ in this study at 180 °C/6 h is shown in Figure 4a. Its shape is spherical, the same as in the 170 °C/4 h study. However, it is different from the shape at 180 °C/24 h, and it is known that the constant temperature time affects the morphology. From the sample results obtained in the process of this study (in the FE-SEM image in Figure 4a), pure $BiVO_4$ appears as small spheres. The shapes of the particles changed from small spheres to rectangles due to the doping of 1 at%Tb in the structural transition from monoclinic to tetragonal (Figure 4b) [37]. As the content of Tb^{3+} atomic percent increases, the rectangular structure gradually disappears

and dissolves and recrystallizes into dispersed particles with a few rods (Figure 4b–d) [33]. The elemental mapping image (Figure 5) of the sample with Tb at 5 atomic percent is shown. O, Tb, Bi, and V were detected, and the four elements were uniformly distributed in the sample, which also strengthened the confirmation that Tb was successfully doped into $BiVO_4$ [38].

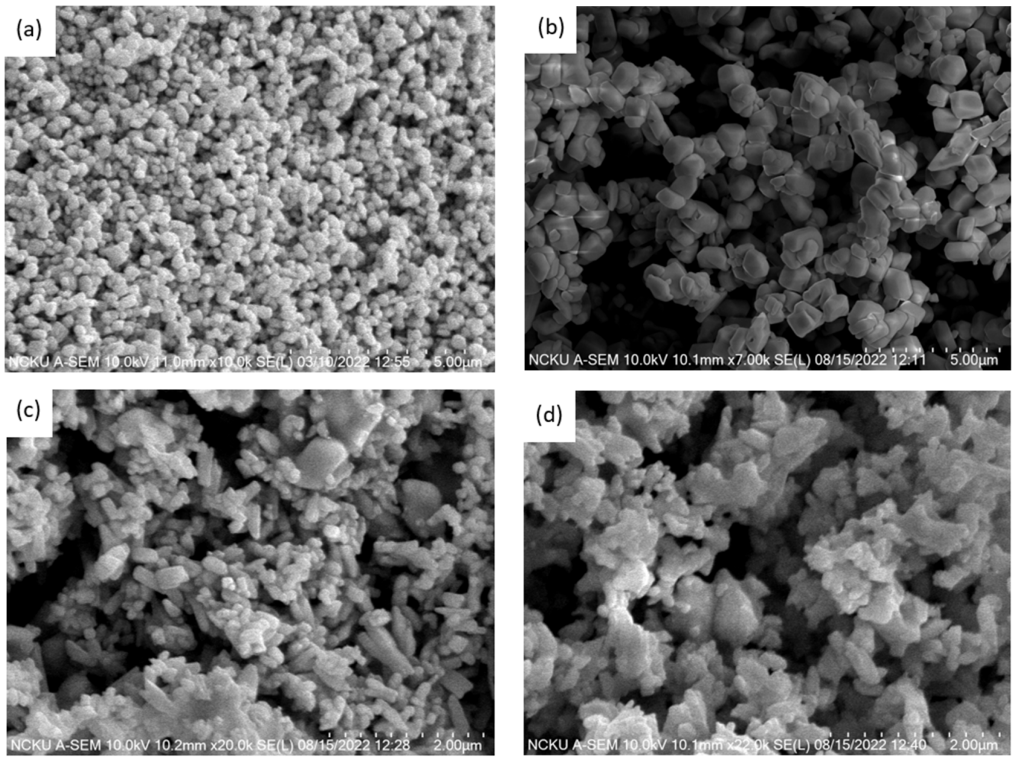

Figure 4. FE-SEM images of (**a**) $BiVO_4$; (**b**) 1%Tb-$BiVO_4$; (**c**) 3%Tb-$BiVO_4$; and (**d**) 5%Tb-$BiVO_4$ samples.

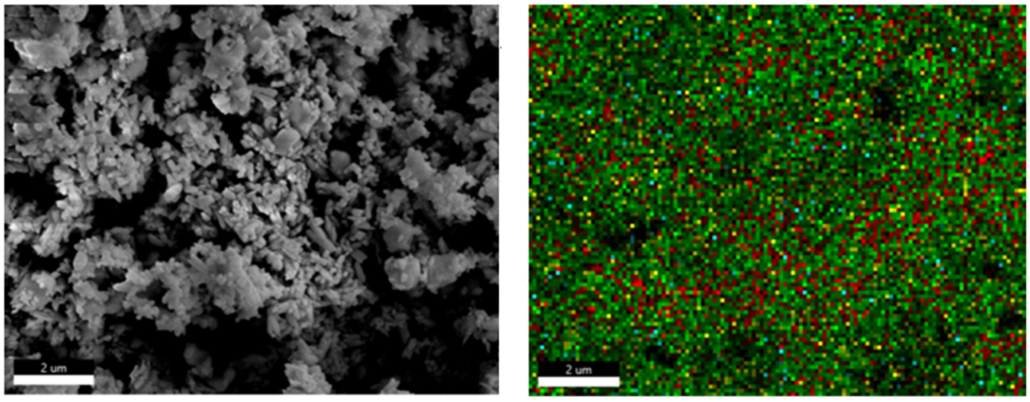

Figure 5. *Cont.*

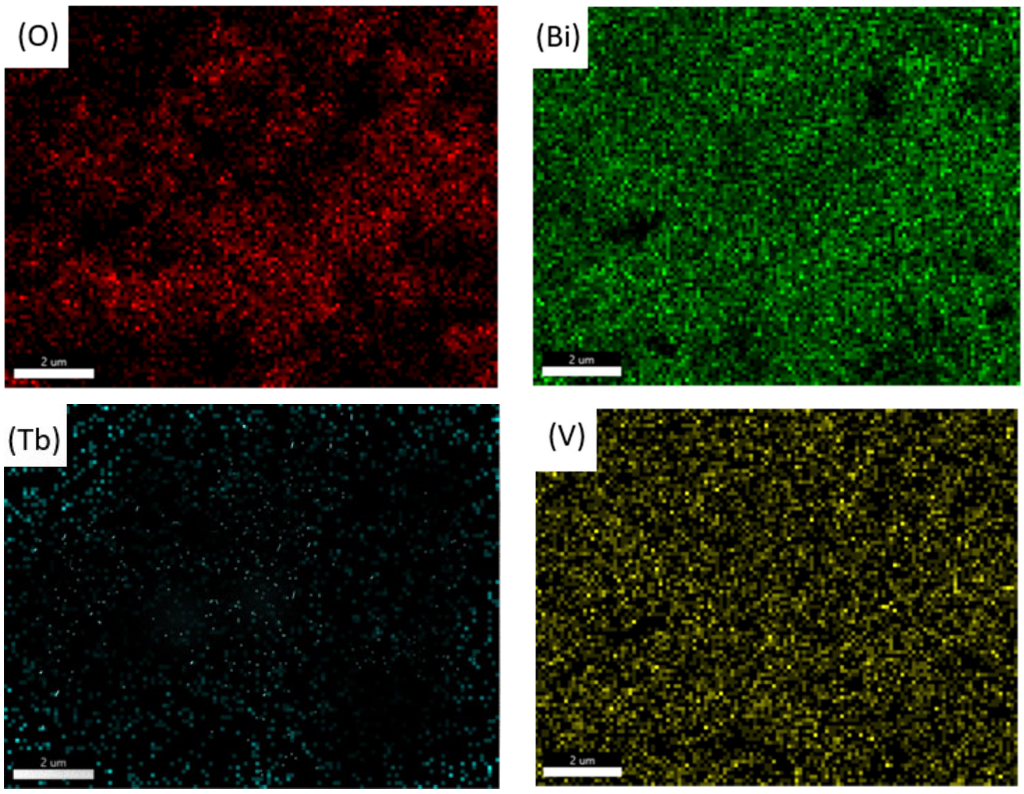

Figure 5. Elemental mapping images of Tb-doped $BiVO_4$.

3.3. Ultraviolet (UV)—Visible Absorption Spectra and Photocatalysis Analysis

It is well known that the light absorption ability of a semiconductor determines its photocatalytic performance. Figure 6a displays the UV-Vis diffuse reflectance spectra for all samples. $BiVO_4$ has an absorption peak in the visible region of 400–600 nm [32]. Compared with undoped $BiVO_4$, Tb-doped $BiVO_4$ has a blue shift (the absorption edge moves to a lower wavelength). The results show the same phase transition from monoclinic to tetragonal as in XRD [32]. The bandgaps of all prepared samples are shown in Figure 6b and Table 3 obtained from $(\alpha h\nu)^2$ vs. $(h\nu)$. The band gap energies of $BiVO_4$, 1at%Tb-$BiVO_4$, 3at%Tb-$BiVO_4$, and 5at%Tb-$BiVO_4$ are 2.37, 2.29, 2.29, and 2.79 eV, respectively. These results are similar to previous reports [32], where the change in bandgap energy indicated that the electronic structure of $BiVO_4$ changed with the phase transition [36].

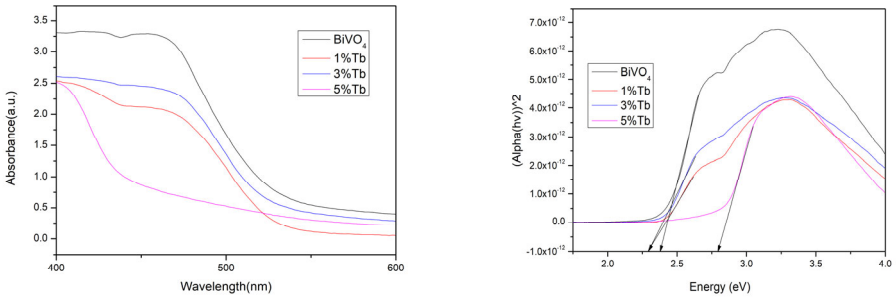

(**a**) (**b**)

Figure 6. (**a**) UV–Vis DRS of the photocatalysts; (**b**) plots of $(\alpha h\nu)^2$ versus hν.

Table 3. Band gap energies of the samples.

Sample	$BiVO_4$	1%Tb	3%Tb	5%Tb
Band gap	2.37	2.29	2.29	2.79

3.4. Degradation Efficiency

Methylene blue was used as a degradation indicator for organic dyes, and the relationship between MB concentration and irradiation time was investigated. The photocatalytic performance of pure $BiVO_4$ and doped $BiVO_4$ samples is shown in Figure 7. After 150 min of xenon arc irradiation, the degradation percentages for the four composites can be calculated by Equation (3). The degradation efficiencies of $BiVO_4$ samples with different atomic percentages of Tb (at% = 0, 1, 3, and 5) were 17.9%, 78.8%, 94.3%, and 61.9%, respectively. Although 5%Tb has the highest atomic percentage, it does not have better degradation efficiency. The sample of 3at%Tb-doped $BiVO_4$ showed the highest photocatalytic performance among all samples [38]. It can be seen that the change in the crystal structure affects photocatalytic efficiency. The doping of Tb^{3+} in $BiVO_4$ also greatly improved the photocatalytic activity [32]. Compared with simple monoclinic and tetragonal crystal systems, the improvement in photocatalytic efficiency depends on the formation of monoclinic and tetragonal $BiVO_4$ heterostructures doped with Tb^{3+}, which helps to improve the separation efficiency of photogenerated charge pairs [32]. From Equation (1), it can be calculated that the ka values of $BiVO_4$, 1%Tb, 3%Tb, and 5%Tb are 1.31×10^{-3}, 1.03×10^{-2}, 1.90×10^{-2}, and 6.43×10^{-3} min^{-1} g^{-1}. The BET surface areas (S_{BET}) of each composite were 4.41, 5.34, 5.63, and 5.72 m^2 g^{-1}, respectively. This corresponds to $BiVO_4$, 1%Tb, 3%Tb, and 5%Tb. The normalized rate constants for each composite are obtained from Equation (2). Finally, k_n is 2.97×10^{-4}, 1.93×10^{-3}, 3.39×10^{-3}, and 1.12×10^{-3} min^{-1} m^{-2} for $BiVO_4$, 1%Tb, 3%Tb and 5%Tb, respectively. From k_n, it can be known that, in the area of degradation efficiency, the influence of the crystal system is more than that of specific surface area. This is because, after excluding the influence of the specific surface area, the normalized kinetic constant of sample 3%Tb is still the largest. Five tests were performed under the same experimental conditions, as shown in Figure 7, to test the stability of the 3at%Tb-doped $BiVO_4$ photocatalyst. The results in Figure 8 show that the degradation percentage of MB in the presence of 3at%Tb-$BiVO_4$ composites continues to be stable [31]. According to other degradation studies, $BiVO_4$ can degrade many kinds of dyes [35], and the degradation efficiency of $BiVO_4$ has different potencies with different ion dopings [31,33].

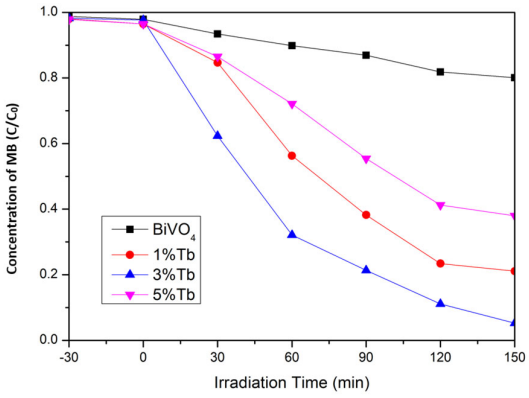

Figure 7. Pure $BiVO_4$ and doped $BiVO_4$ samples degraded MB at different time intervals.

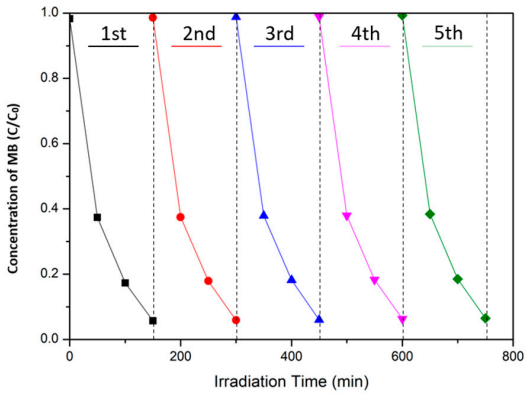

Figure 8. Cycling runs in the photodegradation of MB by monoclinic 3at%Tb-$BiVO_4$ under simulated sunlight.

3.4.1. The Effect of Photocatalyst Addition on the Degradation of Methylene Blue

Degradation efficiency is closely related to the amount of photocatalyst. In this study, 10 mL and 10 ppm of methylene blue were used, 3%Tb was used as a sample in a neutral environment, and photocatalyst addition was adjusted to 5, 10, 15, 20, and 25 mg to compare degradation efficiencies. As shown in Figure 8, it can be found that, when the amount of photocatalyst added is increased to 10, 15, or 20 mg, the degradation efficiency after 90 min of irradiation is significantly improved, from 89.9% to 96.7%. The reaction kinetic constant also increased from 1.52×10^{-2} to 2.27×10^{-2}. When the addition increased to 25 mg, photocatalytic efficiency did not improve. It can be seen from the kinetic constant that it declined. The degradation efficiency is even lower than the kinetic constant with a 5 mg addition. The result is that the more photocatalysts are added within a specific range the higher the degradation rate will be. However, if it exceeds the range, light will be blocked by excessive added photocatalyst particles, and the efficiency of light energy capture on the surface of the photocatalyst will become low. The active site density of surface electrons and holes decreases, so that degradation efficiency does not increase but decreases [39]. It is known that the best photocatalyst addition amount is 20 mg. In the experiments in the latter section, a 3%Tb sample with the optimal parameter of 20 mg was used. Figures 9 and 10 shows the degradation efficiency and its kinetic constant.

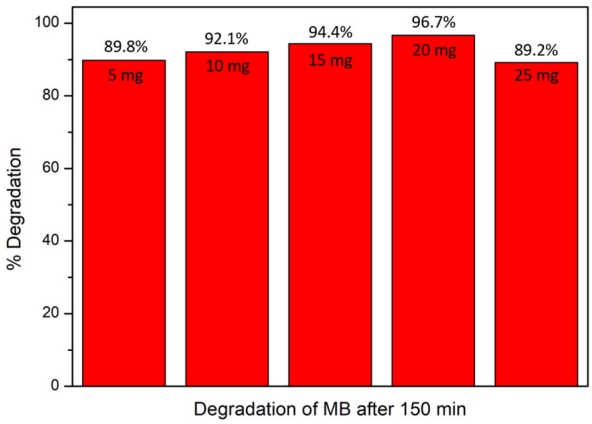

Figure 9. Degradation rates of MB with different added amounts of 3%Tb.

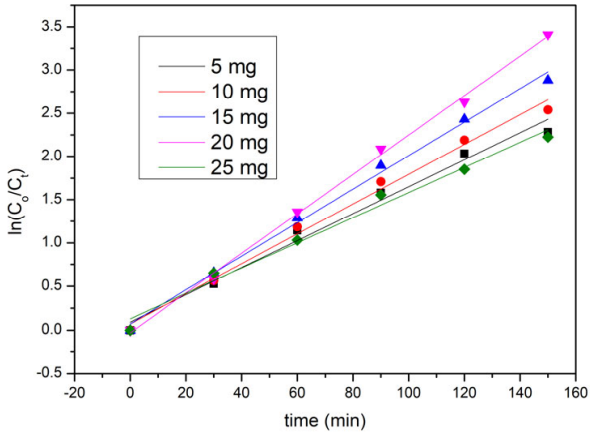

Figure 10. Graph of $\ln(C_0/C_t)$ versus time for 3%Tb added in different amounts.

3.4.2. Effect of the Initial Concentration of Methylene Blue on Photocatalytic Degradation Efficiency

To understand the effect of the initial concentration of dye on the results of the degradation experiments, five concentrations (5, 10, 15, 20, and 25 ppm) of methylene blue were formulated. A total of 20 mg of 3%Tb sample was used for degradation in an environment of pH = 7. The result is shown in Figure 10. After 150 min of visible light irradiation, the degradation efficiencies of MB were 96.5% at 5 ppm, 94.7% at 10 ppm, 86.6% at 15 ppm, 81.9% at 20 ppm, and 75.2% at 25 ppm. Based on these results, with an increase in dye concentration, degradation efficiency decreased. Due to the reduction in the total amount of photon penetration used to excite the photocatalyst, this affects the generation of electron holes. It also affects the absorption of photons because the path lengths of photons entering the solution are reduced. This also indicates that, as the initial concentration of the dye increases, a larger specific surface area is required. The results are consistent with the effects of dye concentration in a study by Matthews [40]. Figures 11 and 12 shows the degradation efficiency and its kinetic constant.

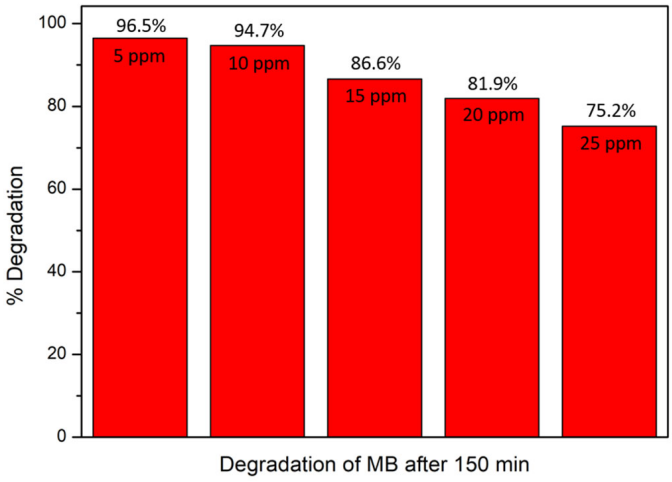

Figure 11. Degradation efficiencies under different concentrations of MB.

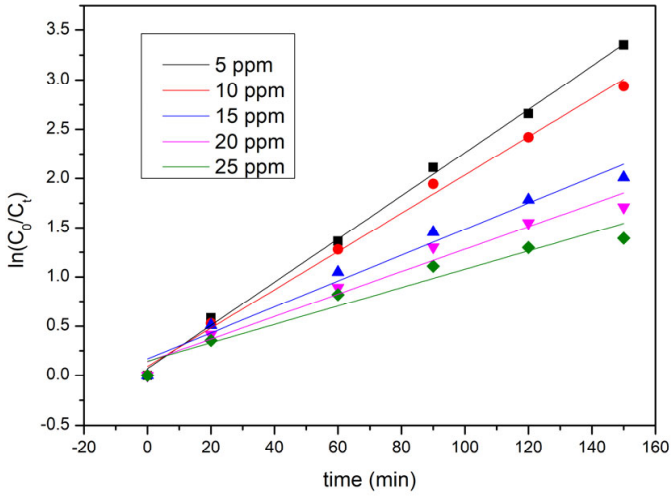

Figure 12. $\ln(C_0/C_t)$ plotted against time at different concentrations of MB.

3.4.3. Effects of Metal Ions and Inorganic Salts on the Degradation Efficiency of Methylene Blue

Metal ions and inorganic salts exist in industrial wastewater. It is relatively important to understand their influence on the efficiency of photocatalytic degradation. This can better simulate real industrial waste liquids. The experiment in this section discusses the effects of metal ions and inorganic salts on degradation efficiency. The analysis was carried out using the optimal addition parameters and concentrations from the previous two sections. Three groups of 10 mL and 5 ppm MB were prepared in an environment of pH = 7. Three groups of dyes were added, with 1.5, 3, and 4.5 g/L mixed solutions of copper sulfate ($CuSO_4$), iron sulfate ($FeSO_4$), and sodium sulfate ($NaSO_4$), respectively. The highest degradation efficiency occurred when the added amount was 1.5 g/L. Degradation efficiency reached 70.2%. In the presence of low concentrations of $FeSO_4$, $CuSO_4$, and $NaSO_4$, the degradation rate did not decrease rapidly, because these ions have an oxidation mechanism under the irradiation of visible light, and the reaction is as follows (taking copper sulfate as an example):

$$CuSO_4 \rightarrow 2Cu^{2+} + {SO_4}^{2-}$$

$${SO_4}^{2-} + OH^0 \rightarrow {SO_4}^0 + OH^-$$

$$2{SO_4}^0 \rightarrow S_2O8^{2-} + 2e^-$$

$${So_4}^0 + \text{dye} \rightarrow {SO_4}^{2-} + \text{dye}^0 \text{ (intermediate)}$$

$${SO_4}^0 + \text{dye}^0 \text{ (Intermediate)} \rightarrow {SO_4}^{2-} + CO_2 + \text{Other Inorganics}$$

Sulfate ions are a strong oxidizing agent. More hydroxyl groups are generated in the dye so that the degradation efficiency of the photocatalyst for the dye is enhanced [41]. Although metal ions such as Cu^{2+}, Fe^{2+}, and Na^+ will be partially adsorbed on the surface of the photocatalyst, affecting the active sites of the photocatalyst, the decrease in photocatalyst efficiency is not obvious when the amount of inorganic salts added is constant. With larger additions of inorganic salts, the degradation efficiency decreases rapidly. Due to the salting-out effect caused by too much salt, the interactions between dyes, electrons, and OH radicals are disturbed. Their degradation efficiencies, from high to low, are 70.2%, 61.7%, and 51.5%. These results indicate that the more metal ions and inorganic salts, the lower

the degradation efficiency [42]. Figures 13 and 14 shows the degradation efficiency and its kinetic constant.

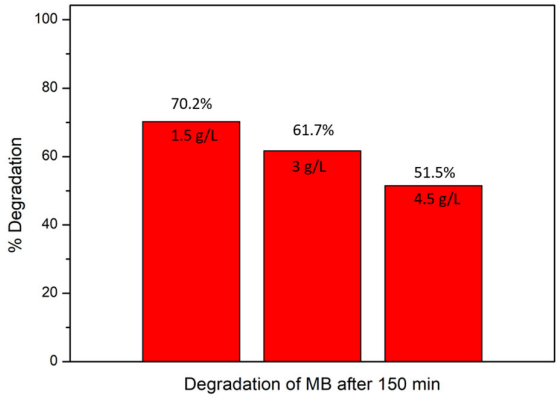

Figure 13. The degradation efficiency of methylene blue containing different concentrations of metal ions and inorganic salts.

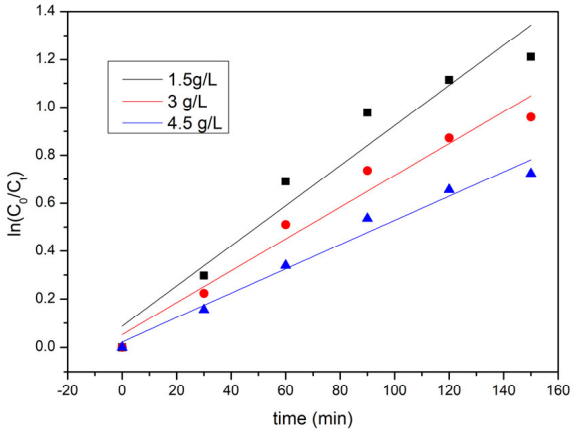

Figure 14. The plot of $\ln(C_0/C_t)$ versus time under different concentrations of metal ions and inorganic salts.

3.4.4. Effect of Solution pH on Photocatalytic Degradation of Methylene Blue

Wastewater containing organic dyes is usually discharged at different pH values. In this section, the experiment compares the effects of the initial pH values of the dye on degradation efficiency. Methylene blue (10 mL, 5 ppm) was used with six pH values (5, 6, 7, 8, 9, and 10). Degradation was performed using 20 mg of Tb3%. It can be seen from the experimental results (Figure 15) the degradation rate increased from acidic to alkaline after 30 min of visible light irradiation. The highest degradation efficiency was found at pH = 9, and the kinetic constants for the pH values from acid to base were 1.34×10^{-2}, 1.69×10^{-2}, 2.25×10^{-2}, 2.54×10^{-2}, 2.67×10^{-2}, and 2.45×10^{-2}. When the pH is greater than 9, OH radicals are partially scavenged. The degradation and reduction availability of MB is then reduced. When the pH values are below 9, there is an electrostatic interaction between the catalyst surface and the dye anion. Metal particles have strong adsorption under alkaline conditions [43]. MB is a cationic dye. Due to the presence of excess protons in acidic conditions, degradation efficiency will be reduced. In an environment of pH = 5, the degradation efficiency is only 86.8%. Figures 15 and 16 shows the degradation efficiency and its kinetic constant.

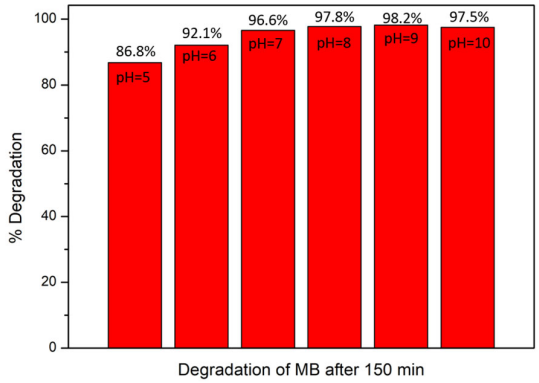

Figure 15. Degradation efficiency of methylene blue at different pH values.

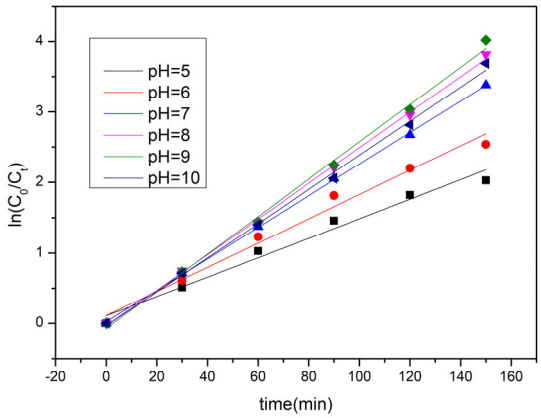

Figure 16. Plotting $\ln(C_0/C_t)$ versus time at different pH values.

4. Conclusions

This study shows that monoclinic and tetragonal mixed $BiVO_4$ products doped with different atomic percentages of Tb were prepared using the hydrothermal method. The photocatalytic activities of the samples all developed in a positive direction. It was found that doping with different atomic percentages of Tb^{3+} can prepare $BiVO_4$ samples with different crystal phases and morphologies. Doping 1 atomic percent and 3 atomic percent Tb is beneficial to the coexistence of monoclinic/tetragonal heterostructures. Compared with undoped $BiVO_4$, the absorption edges of Tb-doped $BiVO_4$ samples shifted to lower wavelengths and changed their energy gaps, which is also closely related to their structural transition. The separation of photogenerated electron–hole pairs was optimized by adding an appropriate amount of Tb, resulting in higher photocatalytic activity. Increases in the initial concentration of the dye, pH value, metal ions, and inorganic salts all have adverse effects on degradation efficiency. Sample Tb3% remained stable in five consecutive degradations. Adding 20 mg with a dye pH value of 9 and an initial dye concentration of 5 ppm achieves the highest degradation efficiency, and photocatalytic efficiency can reach 98.2%. A Tb-doped $BiVO_4$ photocatalyst can process organic dyes for environmental protection purposes and applications. In the future, we plan to recover zinc from waste materials and incorporate it into our doping experiments.

Author Contributions: Conceptualization, M.-H.W. and J.-Y.W.; data curation, M.-H.W.; formal analysis, M.-H.W.; investigation, M.-H.W.; methodology, W.-S.C., M.-H.W., and J.-Y.W.; resources, W.-S.C.; supervision, W.-S.C. and J.-Y.W.; validation, J.-Y.W.; visualization, M.-H.W.; writing—original draft, M.-H.W.; writing—review and editing, J.-Y.W. All authors have read and agreed to the published version of the manuscript.

Funding: This research received no external funding.

Institutional Review Board Statement: Not applicable.

Informed Consent Statement: Not applicable.

Data Availability Statement: Not applicable.

Acknowledgments: We are pleased to acknowledge the support of the Laboratory of Resource Circulation (LRC) at the National Cheng Kung University.

Conflicts of Interest: The authors declare no conflict of interest.

References

1. Benny, C.K.; Chakraborty, S. Dyeing wastewater treatment in horizontal-vertical constructed wetland using organic waste media. *J. Environ. Manag.* **2023**, *331*, 117213. [CrossRef]
2. Nabih, M.H.; El Hajam, M.; Boulika, H.; Chiki, Z.; Tahar, S.B.; Kandri, N.I.; Zerouale, A. Preparation and characterization of activated carbons from cardoon "Cynara Cardunculus" waste: Application to the adsorption of synthetic organic dyes. *Mater. Today Proc.* **2022**, *72*, 3369–3379. [CrossRef]
3. Zhu, X.; Zhang, J.; Chen, F. Study on visible light photocatalytic activity and mechanism of spherical $Bi_{12}TiO_{20}$ nanoparticles prepared by low-power hydrothermal method. *Appl. Catal. B Environ.* **2011**, *102*, 316–322. [CrossRef]
4. Hoang, S.; Guo, S.; Hahn, N.T.; Bard, A.J.; Mullins, C.B. Visible light driven photoelectrochemical water oxidation on nitrogen-modified TiO_2 nanowires. *Nano Lett.* **2012**, *12*, 26–32. [CrossRef] [PubMed]
5. Fujishima, A.; Honda, K. Electrochemical photolysis of water at a semiconductor electrode. *Nature* **1972**, *238*, 37–38. [CrossRef] [PubMed]
6. Lasek, J.; Yu, Y.H.; Wu, J.C. Removal of NOx by photocatalytic processes. *J. Photochem. Photobiol. C Photochem. Rev.* **2013**, *14*, 29–52. [CrossRef]
7. Ran, J.; Jaroniec, M.; Qiao, S.Z. Cocatalysts in semiconductor-based photocatalytic CO_2 reduction: Achievements, challenges, and opportunities. *Adv. Mater.* **2018**, *30*, 1704649. [CrossRef] [PubMed]
8. Nandhini, N.T.; Rajeshkumar, S.; Mythili, S. The possible mechanism of eco-friendly synthesized nanoparticles on hazardous dyes degradation. *Biocatal. Agric. Biotechnol.* **2019**, *19*, 101138. [CrossRef]
9. Liu, G.Y.; Li, K.K.; Jia, J.I.A.; Zhang, Y.T. Coal-based graphene as a promoter of TiO_2 catalytic activity for the photocatalytic degradation of organic dyes. *New Carbon Mater.* **2022**, *37*, 1172–1180. [CrossRef]
10. Voisin, H.; Faloura, X.; Rivard, C.; Capron, I. Versatile nanocellulose-anatase TiO_2 hybrid nanoparticles in Pickering emulsions for the photocatalytic degradation of organic and aqueous dyes. *JCIS Open* **2021**, *3*, 100014. [CrossRef]
11. Madima, N.; Kefeni, K.K.; Mishra, S.B.; Mishra, A.K. TiO_2-modified g-C_3N_4 nanocomposite for photocatalytic degradation of organic dyes in aqueous solution. *Heliyon* **2022**, *8*, e10683. [CrossRef] [PubMed]
12. Mottola, S.; Mancuso, A.; Sacco, O.; De Marco, I.; Vaiano, V. Production of hybrid TiO_2/β-CD photocatalysts by supercritical antisolvent micronization for UV light-driven degradation of azo dyes. *J. Supercrit. Fluids* **2022**, *188*, 105695. [CrossRef]
13. Sukhoverkov, K.V.; Le-Deygen, I.M.; Egorov, A.M.; Kudryashova, E.V. Physicochemical properties of the inclusion complex of moxifloxacin with hydroxypropyl-β-cyclodextrin synthesized by RESS. *Russ. J. Phys. Chem. B* **2018**, *12*, 1193–1204. [CrossRef]
14. Hanna, K.; De Brauer, C.; Germain, P. Cyclodextrin-enhanced solubilization of pentachlorophenol in water. *J. Environ. Manag.* **2004**, *71*, 1–8. [CrossRef] [PubMed]
15. Razavi-Khosroshahi, H.; Mohammadzadeh, S.; Hojamberdiev, M.; Kitano, S.; Yamauchi, M.; Fuji, M. $BiVO_4$/BiOX (X = F, Cl, Br, I) heterojunctions for degrading organic dye under visible light. *Adv. Powder Technol.* **2019**, *30*, 1290–1296. [CrossRef]
16. Yin, W.; Wang, W.; Zhou, L.; Sun, S.; Zhang, L. CTAB-assisted synthesis of monoclinic $BiVO_4$ photocatalyst and its highly efficient degradation of organic dye under visible-light irradiation. *J. Hazard. Mater.* **2010**, *173*, 194–199. [CrossRef]
17. Wang, M.; Niu, C.; Liu, J.; Wang, Q.; Yang, C.; Zheng, H. Effective visible light-active nitrogen and samarium co-doped $BiVO_4$ for the degradation of organic pollutants. *J. Alloys Compd.* **2015**, *648*, 1109–1115. [CrossRef]
18. Bashir, S.; Jamil, A.; Khan, M.S.; Alazmi, A.; Abuilaiwi, F.A.; Shahid, M. Gd-doped $BiVO_4$ microstructure and its composite with a flat carbonaceous matrix to boost photocatalytic performance. *J. Alloys Compd.* **2022**, *913*, 165214. [CrossRef]
19. Zhang, S.; Ou, X.; Yang, X.; Wang, D.; Zhang, C. Preparation and properties of Al^{3+}-doped $BiVO_4$ semiconductor photocatalyst. *Chem. Phys. Lett.* **2021**, *778*, 138747. [CrossRef]
20. Xu, G.; Du, M.; Zhang, J.; Li, T.; Guan, Y.; Guo, C. Facile fabrication of magnetically recyclable Fe_3O_4/$BiVO_4$/CuS heterojunction photocatalyst for boosting simultaneous Cr (VI) reduction and methylene blue degradation under visible light. *J. Alloys Compd.* **2022**, *895*, 162631. [CrossRef]
21. Obregón, S.; Colón, G. Improved O_2 evolution from a water splitting reaction over Er^{3+} and Y^{3+} co-doped tetragonal $BiVO_4$. *Catal. Sci. Technol.* **2014**, *4*, 2042–2050. [CrossRef]
22. Jin, Z.; Zhang, Y.; Liu, D.; Ding, H.; Mamba, B.B.; Kuvarega, A.T.; Gui, J. Fabrication of a La-doped $BiVO_4$@ CN step-scheme heterojunction for effective tetracycline degradation with dual-enhanced molecular oxygen activation. *Sep. Purif. Technol.* **2021**, *277*, 119224. [CrossRef]
23. Zhang, Y.; Yi, Z.; Wu, G.; Shen, Q. Novel Y doped $BiVO_4$ thin film electrodes for enhanced photoelectric and photocatalytic performance. *J. Photochem. Photobiol. A Chem.* **2016**, *327*, 25–32. [CrossRef]

24. Luo, X.L.; Liu, C.J.; Chen, M.J.; Zhang, S.S.; Xu, Y.H. Electrochemical performance and enhanced photocatalytic activity of Ce-doped $BiVO_4$ under visible light irradiation. *Mater. Res. Bull.* **2017**, *94*, 428–434. [CrossRef]
25. Xue, S.; He, H.; Wu, Z.; Yu, C.; Fan, Q.; Peng, G.; Yang, K. An interesting Eu, F-codoped $BiVO_4$ microsphere with enhanced photocatalytic performance. *J. Alloys Compd.* **2017**, *694*, 989–997. [CrossRef]
26. Wang, M.; Han, J.; Lv, C.; Zhang, Y.; You, M.; Liu, T.; Li, S.; Zhu, T. Ag, B, and Eu tri-modified $BiVO_4$ photocatalysts with enhanced photocatalytic performance under visible-light irradiation. *J. Alloys Compd.* **2018**, *753*, 465–474. [CrossRef]
27. Luo, Y.; Tan, G.; Dong, G.; Ren, H.; Xia, A. A comprehensive investigation of tetragonal Gd-doped $BiVO_4$ with enhanced photocatalytic performance under sun-light. *Appl. Surf. Sci.* **2016**, *364*, 156–165. [CrossRef]
28. Nasiri, S.; Rahimirad, Z.; Dehaghi, M.Y.; Rabiei, M.; Ebrahimi-Kahrizsangi, R.; Palevicius, A.; Janusas, G. Facile synthesis and study of photocatalytic properties of TiO2-Ag-Ce nanocomposites. *Mater. Lett.* **2022**, *322*, 132489. [CrossRef]
29. Prabhavathy, S.; Arivuoli, D. Visible light-induced Silver and Lanthanum co-doped $BiVO_4$ nanoparticles for photocatalytic dye degradation of organic pollutants. *Inorg. Chem. Commun.* **2022**, *141*, 109483. [CrossRef]
30. Gomes, L.E.; Nogueira, A.C.; da Silva, M.F.; Plaça, L.F.; Maia, L.J.; Gonçalves, R.V.; Ullah, S.; Khan, S.; Wender, H. Enhanced photocatalytic activity of $BiVO_4$/Pt/PtOx photocatalyst: The role of Pt oxidation state. *Appl. Surf. Sci.* **2021**, *567*, 150773. [CrossRef]
31. Chen, W.S.; Chen, H.R.; Lee, C.H. The Photocatalytic Performance of Ag-Decorated SiO_2 Nanoparticles (NPs) and Binding Ability between Ag NPs and Modifiers. *Coatings* **2022**, *12*, 146. [CrossRef]
32. Wang, Y.; Liu, F.; Hua, Y.; Wang, C.; Zhao, X.; Liu, X.; Li, H. Microwave synthesis and photocatalytic activity of Tb^{3+} doped $BiVO_4$ microcrystals. *J. Colloid Interface Sci.* **2016**, *483*, 307–313. [CrossRef] [PubMed]
33. Huang, J.; Tan, G.; Zhang, L.; Ren, H.; Xia, A.; Zhao, C. Enhanced photocatalytic activity of tetragonal $BiVO_4$: Influenced by rare earth ion Yb^{3+}. *Mater. Lett.* **2014**, *133*, 20–23. [CrossRef]
34. Mali, S.S.; Park, G.R.; Kim, H.; Kim, H.H.; Patil, J.V.; Hong, C.K. Synthesis of nanoporous Mo: $BiVO_4$ thin film photoanodes using the ultrasonic spray technique for visible-light water splitting. *Nanoscale Adv.* **2019**, *1*, 799–806. [CrossRef] [PubMed]
35. Malathi, A.; Madhavan, J.; Ashokkumar, M.; Arunachalam, P. A review on $BiVO_4$ photocatalyst: Activity enhancement methods for solar photocatalytic applications. *Appl. Catal. A Gen.* **2018**, *555*, 47–74.
36. Bahuleyan, B.K.; Toussaint, K.; Rinnert, H.; Vallon, R.; Molinari, M.; Chuburu, F.; Cadiou, C. Silicon wafer functionalization with a luminescent Tb (III) coordination complex: Synthesis, characterization, and application to the optical detection of NO in the gas phase. *Molecules* **2019**, *24*, 1914. [CrossRef]
37. Noor, M.; Sharmin, F.; Al Mamun, M.A.; Hasan, S.; Hakim, M.A.; Basith, M.A. Effect of Gd and Y co-doping in $BiVO_4$ photocatalyst for enhanced degradation of methylene blue dye. *J. Alloys Compd.* **2022**, *895*, 162639. [CrossRef]
38. Qin, C.; Liao, H.; Rao, F.; Zhong, J.; Li, J. One-pot hydrothermal preparation of Br-doped $BiVO_4$ with enhanced visible-light photocatalytic activity. *Solid State Sci.* **2020**, *105*, 106285. [CrossRef]
39. Saquib, M.; Muneer, M. Semiconductor mediated photocatalysed degradation of an anthraquinone dye, Remazol Brilliant Blue R under sunlight and artificial light source. *Dye. Pigment.* **2002**, *53*, 237–249. [CrossRef]
40. Zang, L.; Liu, C.Y.; Ren, X.M. Photochemistry of semiconductor particles 3. Effects of surface charge on reduction rate of methyl orange photosensitized by ZnS sols. *J. Photochem. Photobiol. A Chem.* **1995**, *85*, 239–245. [CrossRef]
41. Liang, C.; Bruell, C.J.; Marley, M.C.; Sperry, K.L. Persulfate oxidation for in situ remediation of TCE. II. Activated by chelated ferrous ion. *Chemosphere* **2004**, *55*, 1225–1233. [CrossRef] [PubMed]
42. Bhaskar, N.S.; Kadam, A.D.; Biwal, J.J.; Diwate, P.M.; Dalbhanjan, R.R.; Mahale, D.D.; Hinge, S.P.; Banerjee, B.S.; Mohod, A.V.; Gogate, P.R. Removal of Rhodamine 6G from wastewater using solar irradiations in the presence of different additives. *Desalination Water Treat.* **2016**, *57*, 18275–18285. [CrossRef]
43. Majumder, S.; Chatterjee, S.; Basnet, P.; Mukherjee, J. Plasmonic photocatalysis of concentrated industrial LASER dye: Rhodamine 6G. *J. Mol. Liq.* **2022**, *358*, 119138. [CrossRef]